Annals of Biomedical Engineering (© 2008)
DOI: 10.1007/s10439-008-9443-x

Validation of Image-Based Method for Extraction of Coronary Morphometry

Thomas Wischgoll,[1] Jenny Susana Choy,[2] Erik L. Ritman,[3] and Ghassan S. Kassab[2]

[1]Department of Computer Science and Engineering, Wright State University, Dayton, OH, USA; [2]Department of Biomedical Engineering, Surgery, Cellular and Integrative Physiology, Indiana Center for Vascular Biology and Medicine, Indiana University-Purdue University, 2069 Medical Sciences Building, Indianapolis, IN, USA; and [3]Department of Physiology and Biomedical Engineering, Mayo Clinic College of Medicine, Rochester, MN, USA

(*Received 12 January 2007; accepted 18 January 2008*)

Abstract—An accurate analysis of the spatial distribution of blood flow in any organ must be based on detailed morphometry (diameters, lengths, vessel numbers, and branching pattern) of the organ vasculature. Despite the significance of detailed morphometric data, there is relative scarcity of data on 3D vascular anatomy. One of the major reasons is that the process of morphometric data collection is labor intensive. The objective of this study is to validate a novel segmentation algorithm for semi-automation of morphometric data extraction. The utility of the method is demonstrated in porcine coronary arteries imaged by computerized tomography (CT). The coronary arteries of five porcine hearts were injected with a contrast-enhancing polymer. The coronary arterial tree proximal to 1 mm was extracted from the 3D CT images. By determining the centerlines of the extracted vessels, the vessel radii and lengths were identified for various vessel segments. The extraction algorithm described in this paper is based on a topological analysis of a vector field generated by normal vectors of the extracted vessel wall. With this approach, special focus is placed on achieving the highest accuracy of the measured values. To validate the algorithm, the results were compared to optical measurements of the main trunk of the coronary arteries with microscopy. The agreement was found to be excellent with a root mean square deviation between computed vessel diameters and optical measurements of 0.16 mm (< 10% of the mean value) and an average deviation of 0.08 mm. The utility and future applications of the proposed method to speed up morphometric measurements of vascular trees are discussed.

Keywords—Image analysis, CT, Segmentation, Coronary arteries.

Address correspondence to Ghassan S. Kassab, Department of Biomedical Engineering, Surgery, Cellular and Integrative Physiology, Indiana Center for Vascular Biology and Medicine, Indiana University-Purdue University, 2069 Medical Sciences Building, Indianapolis, IN, USA. Electronic mail: gkassab@iupui.edu

INTRODUCTION

The analysis of spatial blood perfusion of any organ requires detailed morphometry on the geometry (diameters, lengths, number of vessels, etc.) and branching pattern (3D angles and connectivity of vessels). Despite the significance of morphometric data for understanding the distribution of blood flow and hemodynamics, the data are relatively sparse. The major reasons for the scarcity of morphometric data are the tremendous labor involved and the necessity to cope with the large amount of data. To reconstruct a vascular structure involving a significant number of vessels in most organs is an extremely labor-intensive endeavor. The solution is to develop a labor-saving methodology for extracting morphometric data from volume rendered images.

Several methods to measure morphometric data, such as vessel diameters, semi-automatically can be found in the literature. Some approaches are based on fitting geometric objects to the data such as generalized cylinders.[40] Since the selected geometric objects are well known, diameters and centerlines can be identified. Other approaches deploy region growing. By using an atlas, Passat *et al.*[35] divided the human brain into different areas to optimize a region growing segmentation of brain vessels. Subsequently,[34] the atlas was refined by adding morphological data, such as vessel diameter and orientation, to extract a vascular tree from phase contrast MRA data. Spaan *et al.*[43] extracted coronary vessels from serially sectioned frozen hearts based on maximum intensity projections and manually determined the dimensions using virtual calipers.

The vessel boundary must be first determined to identify the centerline and compute the radius as the distance between the centerline and the boundary. A number of segmentation approaches are available to

Journal : ABME MS Code : 10439 PIPS No. : 9443 ☐ TYPESET ☑ DISK ☐ LE ☑ CP Dispatch : 22-1-2008 Pages : 13

determine the vessel boundary including surface extraction based on an energy function of the image gradient,[15] deformable meshes,[16] hysteresis thresholding and region growing,[30] and distance to the vessel wall subject to a penalty function.[44]

Once the boundary is extracted, the centerlines can be determined. An overview of available techniques can be found in the paper by Cornea *et al.*[12] For computing centerlines, topology- or connectivity-preserving thinning is a common approach.[38,51,52] Ukil and Reinhardt[48] introduced a smoothing approach for airways of a lung based on an ellipsoidal kernel before segmenting and thinning the 3D volumetric image. By using the Hessian of the image intensity, Bullitt *et al.*[9] developed a ridge line detection method to identify centerlines. The algorithm by Aylward and Bullitt[3] is based on intensity ridge traversal. The resulting centerlines are smoothed using a B-spline-based approach. Zhang *et al.*[54] described a centerline extraction algorithm based on Dijkstra's algorithm using a distance-field cost function.

Once the centerline is determined, quantitative data, such as lengths, areas, and angles, can be extracted.[29,52] A detailed data structure for building an airway tree was described by Chaturvedi and Lee.[11] Recently, Nordsletten *et al.*[31] proposed an approach that segments vessels of rat kidney based on iso-surface computation. Using the surface normals, the surface projects to the center of the vessels, while a snake algorithm collects and connects the resulting point cloud. To analyze the branching morphology of the rat hepatic portal vein tree, Den Buijs *et al.*[8] compared the radii and branching angles of the vessels to a theoretical model of dichotomous branching.

In this study, we introduce a software tool for extracting and measuring tubular objects from volumetric imagery of CT images of porcine coronary arteries. The proposed method identifies the vessels and determines the centerlines of those vessels; i.e., it reduces the entire vasculature to a curve-skeleton. This in turn allows the software to compute the vessel diameter at any given point as the distance between the centerline and the vessel wall. Furthermore, the method is validated against manually determined optical measurements of vessel diameters to assess its accuracy. Hence, this study represents the first validation of a segmentation algorithm with actual vessel casts measured optically.

METHODS

CT Images of Coronary Arteries

Five hearts from normal Yorkshire swine of either sex with body weight of 34.3–42.1 kg were studied. The animals were fasted overnight and ketamine, 20 mg/kg, and atropine, 0.05 mg/kg, were administered intramuscularly before endotracheal intubation. The animals were ventilated using a mechanical respirator and general anesthesia was maintained with 1–2% isoflurane and oxygen. The chest was opened through a midsternal thoracotomy, and an incision was made in the pericardium to reach the heart. The animals were then deeply anesthetized followed by an injection of a saturated KCl solution through the jugular vein to relax the heart. The aorta was clamped to keep air bubbles from entering the coronary arteries, and the heart was excised and placed in a saline solution. The left anterior descending (LAD) artery, the right coronary artery (RCA) and the left circumflex (LCX) artery were cannulated under saline to avoid air bubbles and perfused with cardioplegic solution to flush out the blood. The three major arteries (RCA, LAD, and LCX) were individually perfused at a pressure of 100 mmHg with three different colors of Microfil (Flow Tech Inc., MV-112, MV 117, MV-130) mixed with Cab-O-Sil to block the capillaries resulting in the filling of only the arterial tree down to precapillary levels. After the Microfil was allowed to harden for 45–60 min, the hearts were kept in the refrigerator in saline solution until the day of the CT scan. The scans were made axially (120 mAs 120 kV, $0.6 \times 0.6 \times 1.0$ mm^3) on a 16-slice scanner (Siemens Somatom Sensation 16).

Optical Measurements of Vessel Trunk

After CT scanning of the casts (Fig. 1a), the hearts were immersed and macerated in 30% potassium hydroxide solution for 3–4 days to remove the tissue and obtain a cast of the major coronary arteries and their branches (Fig. 1). The trunk of the LAD, RCA, and LCX casts was then photographed using a dissection microscope and a color digital camera (Nikon). For each photograph, the diameter of the three main trunks were measured at each branch from the proximal artery to where the trunk becomes <1 mm in diameter. The optical measurements of diameters along the length of the trunk were made using SigmaScan Pro 5 software. The measurements were then compared to the values retrieved from the extraction algorithm using the distance to the proximal artery as reference.

Computer-Assisted Extraction of Morphometric Data from CT Volumetric Images

The proposed system extracts morphometric data from a volumetric image in several steps. Although a brief summary of the algorithm is given here, a detailed description can be found in the appendix. As outlined

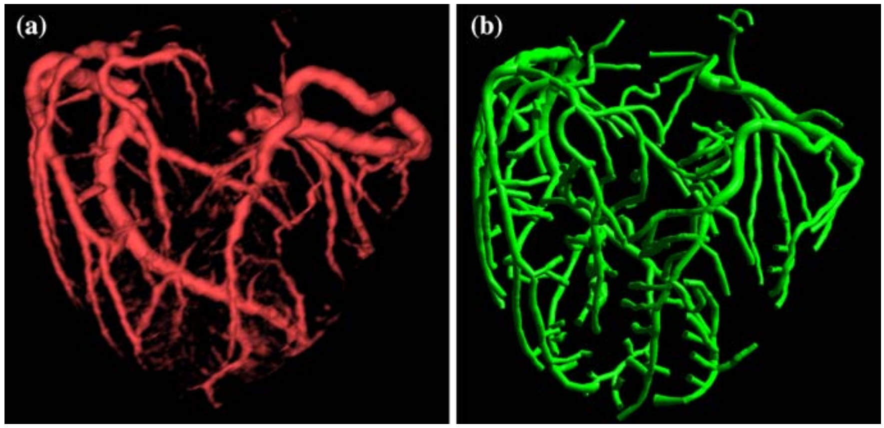

FIGURE 1. (a) Arterial tree of a porcine heart visualized as a volume rendered image with lighting enabled and the (b) reconstructed geometry of the same arterial tree based on centerlines and vessel radii.

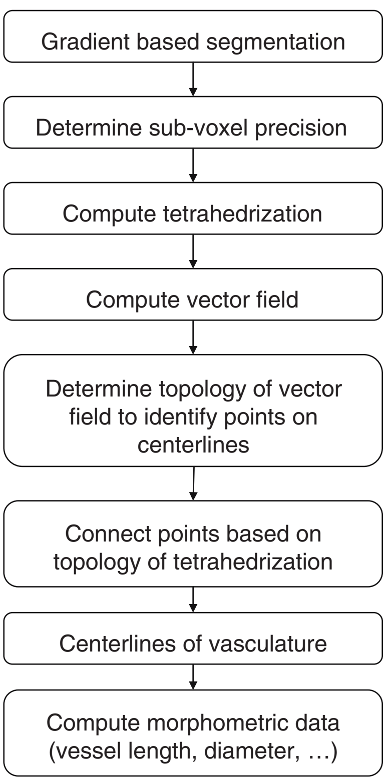

FIGURE 2. Flow chart outlining steps of the segmentation algorithm.

in Fig. 2, the algorithm first segments the vessels within the volumetric image based on the image gradients. In order to get a more accurate representation of the vessel boundary, the points resulting from the segmentation step were moved along the gradient direction in such a way that they were located at the maximal gradient. This provides a more precise and smoother representation at sub-voxel level of the boundary compared to using the original voxel locations. The vectors were then computed for every point on the boundary detected by the previous step in such a way that all vectors were pointing inwards to the center of the vessel. In the simplest case, the image gradients can be used at the boundary. Using a tri-linear interpolation, a vector field covering the inside of the vasculature was computed after a tetrahedrization of all the boundary points was determined. Finally, the points on the centerlines were computed using a topological analysis of the vector field within the cross sectional area of the vessels and connected based on the topology of the tetrahedrization. This then results in a precise representation of the centerlines of all vessels within the volumetric image. Figure 1 depicts a typical data set shown as a volume rendering (Fig. 1a) and a geometric reconstruction based on the centerlines and vessel radii (Fig. 1b) from similar view directions. The vessel diameters were then computed as the distance between the center and the vessel boundary. The major trunk of the artery was defined along the path of the larger diameter at each bifurcation.

Data and Statistical Analysis

In order to facilitate a statistical analysis for the five hearts, the position along the RCA, LAD, and LCX arteries was normalized with respect to the total length (from inlet of artery down to 1 mm diameter). Hence, the results were expressed in terms of fractional longitudinal position (FLP), ranging from 0 to 1. The data for both the independent (FLP) and dependent variables (diameter) were then divided into 20 equal intervals: 0–0.05, 0.06–0.1, 0.11–0.15, …, 0.91–0.95, 0.96–1.0. The results were expressed as means ± 1SD (standard deviation) over each interval. The root mean square (rms) error and average deviation between computer-based and optical measurements were determined. Paired *t*-tests for the three trunks separately were used to detect possible differences between groups and intervals. For this, the average measurements of the optical and computer-based methods for all hearts pooled together were used within each interval.

RESULTS

The algorithm was first validated on a simple, computer-generated phantom dataset that included a tubular-shaped object. Since this data set was computer-generated, the location of the centerlines and the diameters were known and any effects of the scanning step were avoided. The centerline was extracted and the radii determined. This test indicated that both the centerlines as well as the diameters were extracted very accurately at an average error of 0.7% and rms error of 1.1%. For true validation, the coronary arterial CT images were used (Fig. 1). The proposed algorithm extracted the curve-skeleton from the volumetric data set to identify the centerlines of the vessels and to extract morphometric data. The extracted curve-skeleton describes the centerlines of the arterial vessels found within the data set. When using a sub-section of the porcine coronary image, it can be seen that the curve-skeleton is well defined and located at the center of the arterial vessels, as shown in Fig. 3. Based on the centerlines, the vessel lengths were determined as the length of the centerline while the vessel radii were computed as the distance between the centerline and the vessel wall. The overall lengths of the main trunks measured from the beginning of the most proximal artery to the end of approximately 1 mm diameter vessel ranged from 8.4 to 10.7 cm for LCX, 10 to 13.8 cm for LAD, and 11.2 to 18.7 cm for RCA. The average diameters for LAD, LCX, and RCA were determined as 2.52, 2.78, and 3.29 mm, respectively.

In order to validate the results derived from CT images (Fig. 1a), the manual optical measurements were compared to the computed values for the main trunks of the LAD, LCX, and the RCA branches. The distance to the proximal artery was used as a reference to compare the optical diameter measurements to the image-extracted values. Figure 4a shows a typical example of the LAD trunk diameter for one representative heart. Computer-based CT and optical measurements are both plotted together in this graph. The length of this branch down to the point of scan resolution (~1 mm) was 9.9 cm. As can be seen from the two curves, the diameters that were manually measured (dashed) agree with the ones determined by the software system (solid) very well. Figures 4b and 4c show the results for the LCX and RCA branch of the same heart, respectively. The lengths of these branches were 8.4 cm and 11.4 cm, respectively. According to paired *t*-test, the probabilities for no statistically significant difference for the three major trunks were 0.23 (LAD), 0.76 (LCX), and 0.64 (RCA). Hence, there were no statistically significant differences between the two measurements ($p > 0.05$).

In order to facilitate a direct comparison between the manually measured data and the computed values, the data were normalized along the length to a scale between zero and one. The inlet of the artery was identified as zero, while the point at which the trunk reached 1 mm diameter was set to one. Figures 5a–c show a comparison of the manually measured and computer-based diameters for all five hearts. The horizontal bars represent the standard deviation (SD) within each bin with respect to the measured lengths. Similarly, the SD of diameter values within each bin is shown as a vertical bar. The computer-based algorithm sampled more measurements as compared to the optical method. As a result, there is a larger variation in the FLP for the computer-based method. As can be seen from these graphs, the manually measured diameters agree very well with the computer-generated values. There were no statistically significant differences between the two sets of measurements at each interval (paired *t*-test per interval $p > 0.05$, averaged for all five hearts). Furthermore, the rms error between the two measurements of all vessels is 0.16 mm (0.21 mm for LAD, 0.14 mm for LCX, and 0.11 mm for RCA) which is < 10% of the average value with average deviation of 0.08 mm (0.11 mm for LAD, 0.08 mm for LCX, and 0.05 mm for RCA).

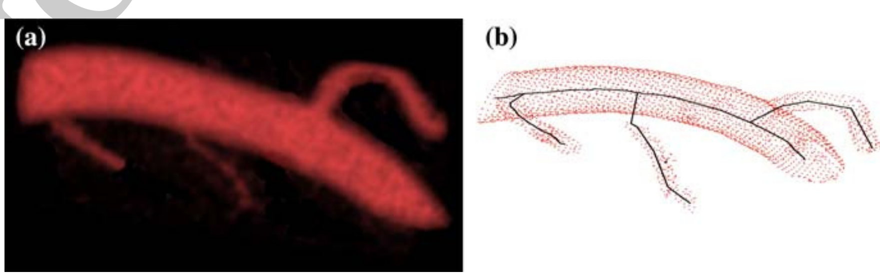

FIGURE 3. (a) A segment of coronary artery cast and (b) extracted curve-skeleton (solid line) of the coronary segment with the vessel boundary indicated by the point cloud.

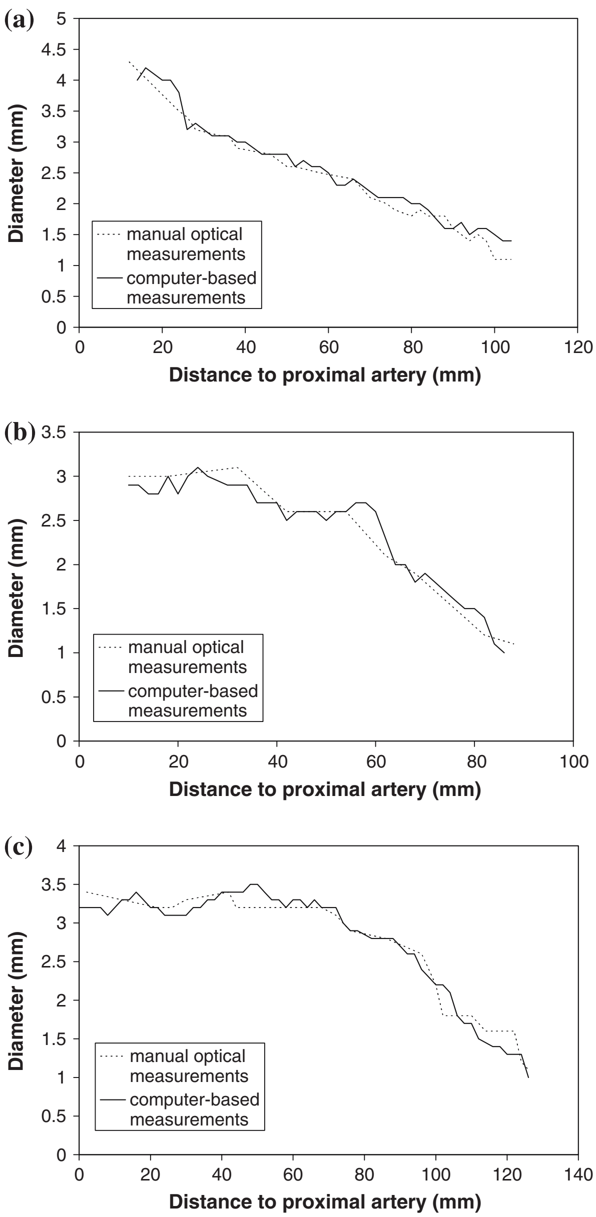

FIGURE 4. A direct comparison between manually measured optical (dashed) and computed (solid) diameters for (a) LAD trunk, (b) LCX trunk, and (c) RCA for a typical specimen. The *x*-axis describes the distance along the trunk, while the *y*-axis corresponds to the diameter.

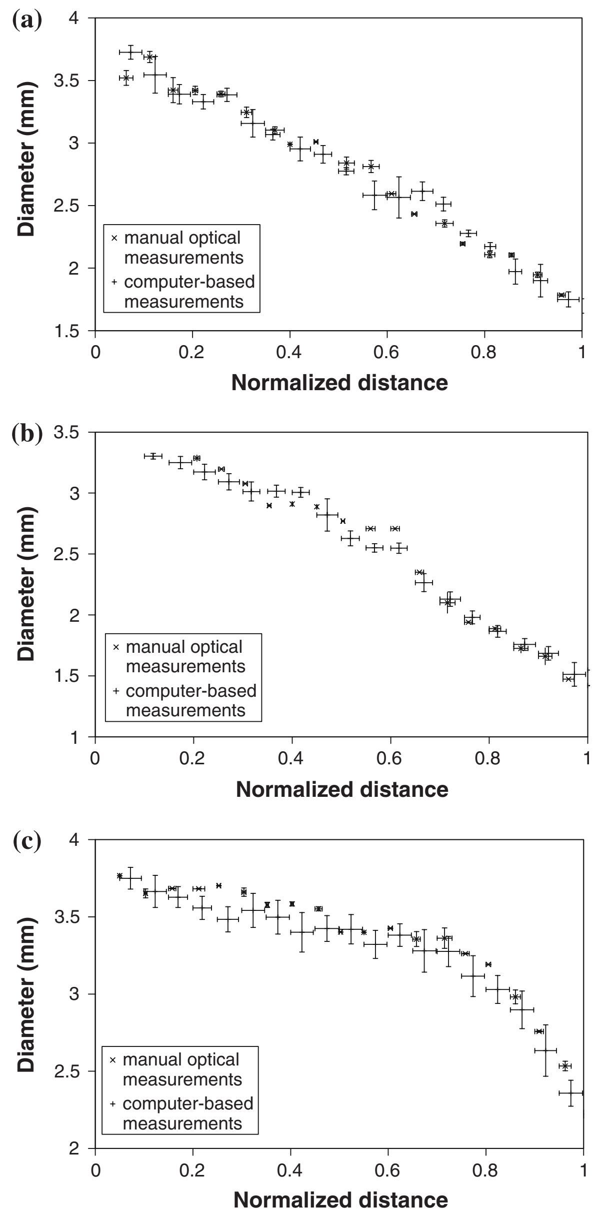

FIGURE 5. Comparison between the manually measured optical (dashed) and computed (solid) diameters for five casts with respect to (a) LAD trunk, (b) LCX trunk, and (c) RCA. The length of the trunk (*x*-axis) was normalized on a scale between 0 and 1, the diameter is shown on the *y*-axis.

DISCUSSIONS

Validation of Image-Based Extraction Algorithm

The algorithm described in this paper utilizes a less computationally intensive method of computing the vector field. Also, the topological analysis of the 2D vector fields within cross-sectional areas of the vessels can be computed more efficiently compared to previous topology-based methods. This allows the software to process a CT scanned data set within a few hours which potentially can be further reduced by optimization of the code. In addition, the proposed algorithm does not require the introduction of artificial starting points for the topological analysis.[13] In fact, the singularities defining the centerlines are generated by projecting the vector field onto the cross-sectional areas of the vessels.

The direct comparison of the diameter values retrieved by extracting the three vessel branches from the CT scanned images and the optical measurements using the cast polymer verify the accuracy of the proposed algorithm. Figure 4 shows the data for the main trunk of a representative vessel. Overall, the two curves for the computed diameters and the measured values agree very well. Once the diameter is <1 mm, the agreement is less satisfactory. This is not surprising since the voxel resolution of the CT scan is about 0.6 mm within the slices and 1.0 mm between slices. Hence, the accuracy of diameters below 1 mm are somewhat questionable since they would be described by less than a single voxels within the volumetric image.

The data in Fig. 5 show the correlation between the averaged optically determined and computed diameters. As can be seen from this figure, the values within each bin are similar for the measured and computed results. We found no statistically significant differences among all bins. The rms error for all hearts is $<10\%$ of the mean diameter which supports the accuracy of the proposed algorithm. The rms error of the measurements computed using the presented technique of 0.16 mm are also more precise compared to other techniques found in the literature,[27] where the rms error ranges from 0.2 to 0.6 mm with scans of similar resolutions ($0.6 \times 0.6 \times 0.6$ mm^3).

Comparison with Other Studies

Some methods begin with all voxels of a volumetric image and use a thinning technique to shrink down the object to a single line.[4,7,18,24,26,32,33,37,47] Ideally, the topology of the object should be preserved as proposed by Lobregt *et al.*[25] which is the basic technique used in commercial software systems, such as Analyze™. The disadvantage of this approach is that it tends to produce jagged lines which do not allow accurate measurements of branch angles. Luboz *et al.*[27] used a thinning-based technique to determine vessel radii and lengths from a CTA scan. A smoothing filter was employed to eliminate the jaggedness of the thinning process and the results were validated using a silicon phantom. A standard deviation of 0.4 mm between the computed and the actual measurements was reported for a scan with similar resolution as that used in this paper. The disadvantage of thinning algorithms is that they can only be applied to volumetric data sets. Since the approach presented in this paper is not based on voxels it can be applied to non-volumetric data; i.e., it is also applicable to geometric data sets, such as those obtained from laser scans. Furthermore, the location of the centerline is determined at a higher numerical precision since the defining points are not bound to a single voxel. This also helps avoid the jagged representation of the centerlines.

Other approaches use the distance transform or distance field in order to obtain a curve-skeleton. For example, fast marching methods[41,46] can be employed to compute the distance field. Voxels representing the centerlines of the object are identified by finding ridges in the distance field. The resulting candidates must then be pruned first. The resulting values are connected using a path connection or minimum span tree algorithm.[45,50,55] The distance field can also be combined with a distance-from-source field to compute a skeleton.[56] Similar to thinning approaches, these methods are voxel-based and tend to generate the same jagged centerlines. This implies that a centerline can deviate from its original location by up to half a voxel due to the numerical representation. The proposed approach does not have this shortcoming as it uses a higher numerical precision for determination of centerlines.

A more recent method by Cornea *et al.*[13] computes the distance field based on a potential similar to an electrical charge and then uses a 3D topological analysis to determine the centerlines. This approach has some disadvantages, however, when applied to CT-scanned volumetric images. For example, it is computationally intensive such that computing the distance field alone would take several months. Furthermore, due to the rare occurrence of 3D singularities used as starting points for topological analysis, additional criteria have to be added. The present algorithm avoids this by linearly interpolating the vector field within the vessels and by performing a 2D topological analysis in cross sections of the vessels only. This results in a significantly shorter computational time for generation of data which is very important for large data sets.

Techniques based on Voronoi diagrams[2,14] define a medial axis using the Voronoi points. Since this approach usually does not result in a single line but rather a surface shaped object, the points need to be clustered and connected in order to obtain a curve-skeleton. Voronoi-based methods can be applied to volumetric images as well as point sets. These methods usually tend to extract medial surfaces rather than single centerlines. Hence, clustering of the resulting points is required which in turn may introduce numerical errors.

For extracting centerlines from volumetric images, geometry-based approaches are preferable over voxel-based approaches. Due to the discrete nature of a voxel of the volumetric image, the location of the centerline can have an error of half a voxel. Geometry-based methods do not have this shortcoming. Nordsletten *et al.*[31] determined normal vectors based on an iso-surface computed using the volumetric image. These normal vectors are projected inward. The resulting point cloud is then collected and connected by a snake algorithm. Since this method estimates the normal vectors, the center of the vessel is not necessarily in the direction of the normal vector. Hence, the computed centerline may not be absolutely accurate. Our proposed technique is based on a vector field analysis with vectors pointing toward the vessel center. This method is more lenient with regard to vector direction while still finding accurate center points. Hence, the proposed technique compensates for this type of error automatically. It is therefore expected that a more precise computation of center points is possible. The approach based on a 3D vector field analysis proposed by Cornea *et al.*[13] results in very accurate computation of the centerlines. The only difficulty with this approach is that computing the centerlines for a CT-scanned volumetric image of the size $512 \times 512 \times 200$ would take several months, which renders it impractical.

Critique of Method

The choice of the initial threshold of the gradient only influences the smallest vessel detected. Hence, a more optimal choice of this threshold can lead to smaller vessels being visualized (limited by the scanner resolution). However, the location of the vessel boundary that is identified by the algorithm is not influenced by this threshold. As a consequence, choosing a different threshold does not change the quantitative measurements and their accuracy. To find an optimal threshold, the first step of the algorithm was executed. If sufficient vessel boundaries were not identified, the threshold was decreased. In case of too much noise, the threshold was increased. After few iterations, an appropriate threshold value was found and the same threshold was used for all data sets.

In some instances, the method fails to connect a smaller vessel to the larger branch at the bifurcation. Since the center lines of the vessels are computed properly, the gap closing step is capable of connecting most of these bifurcations properly. Furthermore, a clear definition of a vessel segment is necessary in order to avoid false bifurcations. Since the proposed algorithm is designed based on topological analysis, a vessel that forks off of a branch is required to have a considerable length in order to be detected. As a result, the presented technique tends to pick up less false bifurcations due to bumps in the vessel boundary compared to algorithms based on Voronoi diagrams. Finally, the present analysis is simplified by casting of the arterial side only without the respective veins. In future studies, algorithms can be established to distinguish and analyze each of the two trees, respectively.

Significance of Study

The present method accurately extracts vascular structures including dimensions (diameters and lengths) from volumetric images. The validation of the computed diameters with optical measurements confirms the accuracy of the method. The algorithm can extract the main trunk as well as the entire vascular tree within the scan resolution. Future applications to the entire tree will allow the determination of vessel diameters and lengths as well as bifurcation angles to reconstruct a realistic anatomy of the vasculature. Such accurate and detailed anatomical models will serve as an architectural platform for hemodynamic analysis of blood flow. The present study is the first step in that direction.

APPENDIX

Computer-Assisted Extraction of Morphometric Data from CT Volumetric Images

The algorithm for extraction of curve-skeletons and determining morphometric data from volumetric images consists of several steps. A detailed description of all steps involved in the algorithm can be found below along with the theoretical framework for the methodology.

Topological Analysis of Vector Fields

The algorithm utilized in this study uses the topology of a vector field defined on the faces of a tetrahedralized set of points. Thus, the vector field is defined by three vectors located at the vertices of a triangle. The vector field inside the triangles is interpolated linearly by computing the barycentric coordinates of the point within the triangle. These coordinates are then used as weights for linearly combining the three vectors defined at the vertices of the triangle to compute the interpolated vector. The advantage of such a linear interpolation is an easier classification of topological features which is briefly described below.

In topological analysis, the zeros of the interpolating vector field are of interest. Synonyms for these zeros are singularities or critical points. Based on the eigenvalues of the matrix of the interpolating vector field, these critical points can be separated into different groups. Within each group, the vector field assumes similar characteristics. Very detailed analysis of these groups and their characteristics can be found in the literature.[20,53] In order to identify points on the centerline, singularities where the vectors point toward that specific point are of interest. These types of singularities are attracting node and focus singularities (both eigenvalues of matrix A are negative), as well as attracting spiral singularities (eigenvalues of matrix A have non-zero imaginary part) as depicted in Fig. 6a–d.

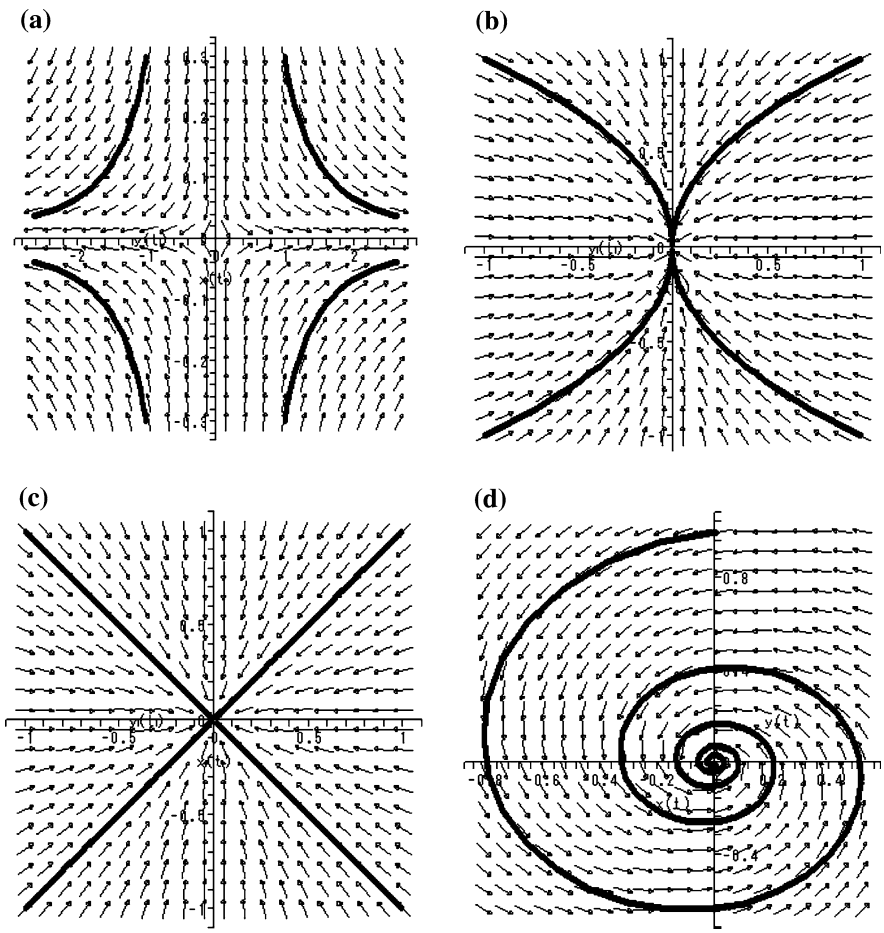

FIGURE 6. Types of singularities that are relevant for topological analysis and for identifying centerlines: (a) saddle singularity of a vector field including surrounding flow depicted by arrow glyphs, (b) node singularity of a vector field including surrounding flow depicted by arrow glyphs, (c) focus singularity of a vector field including surrounding flow depicted by arrow glyphs, and (d) spiral singularity of a vector field including surrounding flow depicted by arrow glyphs.

Methodology for Extraction of Quantitative Information

The algorithm for determination of the curve-skeleton consists of several steps. Since the object is given as a volumetric CT-scanned image, the object boundary must to be extracted first. A vector field is then computed that is orthogonal to the object boundary surface. Once the vector field is computed, the curve-skeleton can be determined by applying a topological analysis to this vector field. As a last step, gaps between segments of the curve-skeleton can be closed automatically and vessel diameters can be computed. The following subsections explain these steps in detail.

Extraction of Object Boundary

The CT-scanned vasculature is defined by a volumetric image. A volumetric image consists of voxels aligned along a regular 3D grid. It is generally not likely that the boundary of the vessels is exactly located at these voxels. Hence, better precision can be achieved by finding the exact location in between a set of voxels. Since an accurate representation of the object boundary is crucial to the algorithm, improvement of the precision is an essential step. The method used within the described system uses similar techniques as described by Canny's non-maxima suppression[10] but extended to three dimensions.

First, the image gradient is computed for every voxel. Using an experimentally determined threshold, all voxels with a gradient length below this threshold are neglected. The gradients of the remaining voxels are then compared to their neighbors to identify local maxima along the gradient. In 3D, the direct neighborhood of a single voxel generally consists of 26 voxels forming a cube that surrounds the current voxel. In order to find the local maximum along the current gradient, the gradients of the neighboring voxels in positive and negative directions have to be determined. When using 2D images, nearest neighbor interpolation of these gradients[21] may work but yield incorrect results in a 3D volumetric image. Therefore, the gradients on the boundary of the cube formed by the neighboring voxels are interpolated linearly to determine a better approximation of the desired gradients. Figure 7a explains this in more detail where the current voxel marked as a triangle and the direct neighbors forming a cube are shown. The current gradient is extended to the faces of the cube starting at the current voxel. The resulting intersections, marked as diamonds, define the locations for which the gradients have to be interpolated so that the maximal gradient can be determined. The current implementation of the described system uses linear interpolation. Using this method, only very few cases require a prefiltering to remove noise in data sets. The best results can be achieved by the use of an anisotropic diffusion filter. The five data sets used in this study were not prefiltered.

Once the neighboring gradients in positive and negative direction of the current gradient are computed, these are compared in order to find the local maxima. Thus, if the length of the current gradient is larger than the length of both of its neighbors, the local maximum can be calculated similar to the 2D case. When interpolated quadratically, the three gradients together form a parabolic curve along the direction of the current gradient as shown in Fig. 7b. In general, the current gradient is larger than the interpolated neighbors since only local maxima are considered in this step. Hence, the local maximum can be identified by determining the zero of the first derivative of the parabolic curve. Determining all local maxima within the volumetric image in this fashion then results in a more accurate and smoother approximation of the object boundary with sub-voxel precision. Once all points on the boundary are extracted from the volumetric image using this gradient approach with sub-voxel precision, the resulting point cloud can be further processed in order to identify the curve-skeleton.

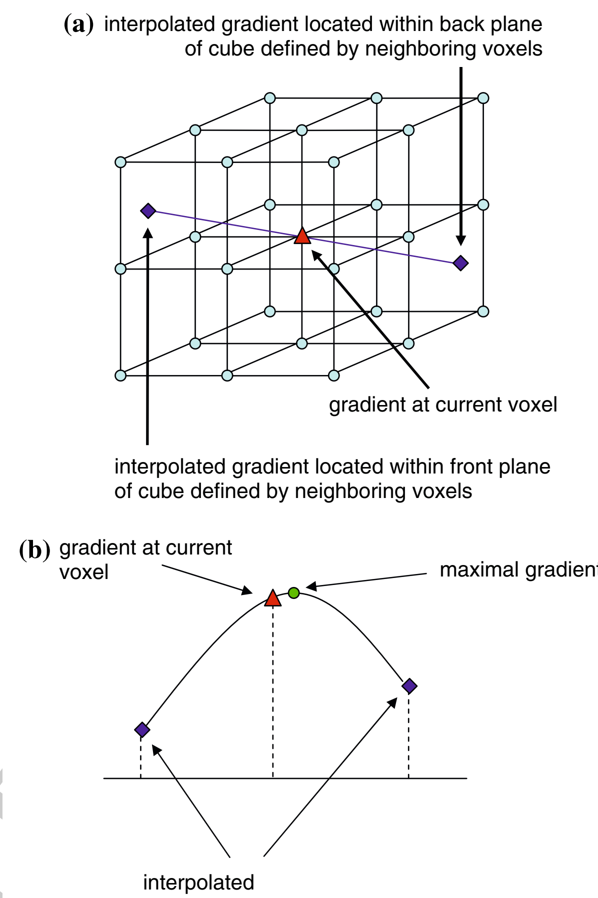

FIGURE 7. (a) Determination of the maximum gradient with sub-voxel precision of a voxel (marked as triangle) and its neighboring voxels: the gradient direction is shown combined with the locations of the interpolated gradients at the intersection of the current gradient direction with the cube defined by the neighboring voxels marked as diamonds. (b) Computation of the local maximum of the gradient (symbolically shown for one coefficient of the gradient vector). The gradient is marked as a triangle and the two interpolated gradients at the edge of the cube are shown as diamonds. The maximal gradient (circle) is determined by computing the zero of the first derivative resulting in the maximum gradient.

Determination of the Vector Field

The proposed method computes a curve-skeleton by applying a topological analysis to a vector field that is determined based on the geometric configuration of the object of which the curve-skeleton is to be determined. The vector field is computed at the identified points on the vessel boundary in such a way that the vectors are orthogonal to the vessel boundary surface. Based on these vectors, the vector field inside the vessels is computed using linear interpolation.

Different approaches are possible for calculating such a vector field. A repulsive force field can be determined that uses the surrounding points on the boundary surface.[13] The repulsive force is defined similarly to the repulsive force of a generalized potential field.[1,22] The basic idea is to simulate a potential field that is generated by the force field inside the object by electrically charging the object boundary. Alternatively, we may define a normal vector and the respective plane. The normal of this plane then defines the orthogonal vector corresponding to the current point.[31]

Since these are volumetric data sets, the image gradients can be used to define the vectors on the boundary surface. These image gradients are previously determined as they are needed for extraction of the boundary. Since the points are only moved along the direction of the image gradient when determining

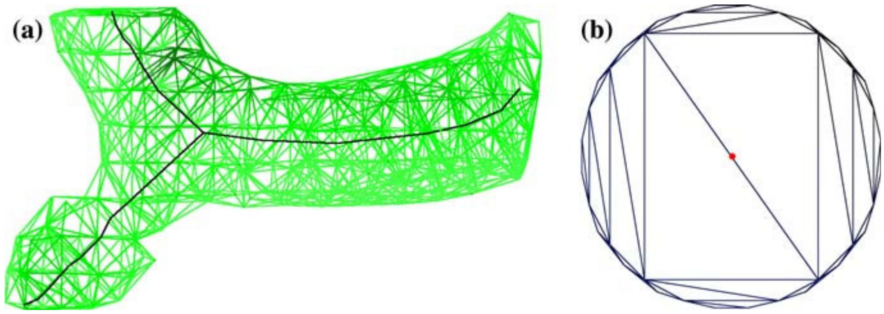

FIGURE 8. (a) A bifurcation for a small vessel (three voxels in diameter). The extracted center line is shown along with the respective tetrahedrization. (b) Single slice through the tetrahedrization of the phantom data set. The point on the centerline is identified in the center of the image.

the sub-voxel precision, this image gradient is still orthogonal to the boundary surface and therefore represents a good approximation for the desired vector field.

The proposed software system uses a Gaussian matrix to compute the image gradients. Therefore, the resulting gradients are smoothed to reduce any remaining noise in the boundary representation. This also reduces the error that occurs whenever gradients are computed close to gaps within the vessel boundary. Due to the use of vector field topology methods for determining center points, the algorithm tends to be less sensitive to errors in the gradients as compared to methods that project the boundary onto the center points directly.[31] In our analysis, gaps within the vessel boundary only occurred for very small vessels with diameters close to the size of a voxel due to partial volume effects. It should be noted that all three methods result in vectors pointing to the inside of the object.

Determination of the Curve-Skeleton

In order to determine the curve-skeleton of the object, a tetrahedrization of all points on the object boundary is computed first. For this, Si's[42] fast implementation of a Delaunay tetrahedrization algorithm is used. This algorithm results in a tetrahedrization of the entire convex hull defined by the set of boundary points. Thus, it includes tetrahedra that are located completely inside the vessels but also tetrahedra that are completely outside of the vessels and connect two vessels. By using the previously computed vectors that point to the inside of the vasculature, outside tetrahedra can be distinguished from tetrahedra that are located inside the vessels. Hence, all outside tetrahedra can be removed, leaving a Delaunay tetrahedrization of the inside of the vasculature only. Note that this step also closes small gaps that may exist since tetrahedra covering these gaps will still have vectors attached to the vertices which point inward. Since vectors are known for each vertex of every tetrahedron, the complete vector field can be computed using this tetrahedrization by linear interpolation within each tetrahedron. This vector field is then used to identify points of the curve-skeleton which are then connected with each other. The vectors of the remaining tetrahedra are non-zero (the tetrahedron would be removed otherwise). Thus, the trivial vector field where the vectors are zero inside the entire tetrahedron does not occur. Figure 8a shows an example of the tetrahedrization with outside tetrahedra removed as previously described for a small vessel with a diameter of about three voxels. Based on this tetrahedrization and associated vector field, the center lines can be identified.

Once the vector field is defined within the entire object, one could use an approach similar to the one used by Cornea *et al.*[13] and compute the 3D topological skeleton of the vector field which yields the curve-skeleton of the object. Since singularities are very rare in a 3D vector field, Cornea *et al.* introduced additional starting points for the separatrices, such as low divergence points and high curvature points, to obtain a good representation of the curve-skeleton. Therefore, a different approach is described in this paper that analyzes the vector field on the faces of the tetrahedra.

In order to perform a topological analysis on the faces of the tetrahedra, the vector field has to be projected onto those faces first. Since tri-linear interpolation is used within the tetrahedra, it is sufficient to project the vectors at the vertices onto each face and then interpolate linearly within the face using these newly computed vectors. Based on the resulting vector field, a topological analysis can be performed on each face of every tetrahedron.

Points on the curve-skeleton can be identified by computing the singularities within the vector field interpolated within every face of the tetrahedrization. For example, for a perfectly cylindrical object, the vector boundary points directly at the center of the cylinder. When examining the resulting vector field at a cross section of the cylinder, a focus singularity is located at the center of the cylinder within this cross section. The location of this focus singularity resembles a point on the curve-skeleton of the cylinder. Hence, a singularity of type node, focus, or spiral within a face of a tetrahedron indicates a point of the curve-skeleton. Since the vectors at the boundary point inwards, only sinks (i.e., attracting singularities) need to be considered in order to identify the curve-skeleton. Since not all objects are cylindrical in shape and given the numerical errors and tolerances, points on the curve-skeleton can be identified from sinks that resemble focus and spiral singularities. Figure 8b illustrates an example for a cylindrical object for which a cross-section (a slice perpendicular to the object) is shown. There are two large triangles that connect two opposite sides of the object. Based on these triangles, which resemble faces of tetrahedra of the tetrahedrization, the center point (shown in red) can be identified based on the topological analysis within these triangles.

Obviously, only faces that are close to being a cross section of the object should be considered in order to identify points on the curve-skeleton. To determine such cross-sectional faces, the vectors at the vertices can be used. If the vectors at the vertices, which are orthogonal to the object boundary, are approximately coplanar with the face, then this face describes a cross section of the object. As a test, the scalar product between the normal vector of the face and the vector at all three vertices can be used. If the result is smaller than a user-defined threshold, this face is used to determine points on the curve-skeleton. If we compute the singularity on one of these faces, then we obtain a point which is part of the curve-skeleton. Note that since linear interpolation is used within the face, only a single singularity can be present in each face. In case of bifurcations, there will be two neighboring tetrahedra which contain a singularity, one for each branch. Additionally, this approach disregards boundary points which are based on noise voxels. In order for a set of boundary points to be considered, they need to have gradient vectors that point toward the center from at least three different directions. Hence, boundary points based on noise voxels are automatically neglected because it is very unlikely that there are other corresponding boundary points in the vicinity with gradient vectors pointing in the direction of the first boundary point.

After computing the center points, the vessel diameters are computed for each center point and all points within the vicinity are identified. From this set of points, only the ones that are within the slice of the vessel used to determine the center point are selected to describe the boundary. The radius is then computed as the average of the distances between the center points and the points on the boundary of the vessel slice.

Once individual points of the curve-skeleton (including the corresponding vessel diameters) are computed by identifying the focus and spiral singularities within the faces of the tetrahedra, this set of points must be connected in order to retrieve the entire curve-skeleton. Since the tetrahedrization describes the topology of the object, the connectivity information of the tetrahedra can be used. Thus, identified points of the curve-skeleton of neighboring tetrahedra are connected with each other forming the curve-skeleton. In some cases, gaps will remain due to the choice of thresholds which can be closed using the method described in the next section.

Closing Gaps within the Curve-Skeleton

Ideally, the method described results in a vascular tree representing the topology of the vasculature exactly. Due to numerical tolerances, however, sometimes gaps may occur between parts of the curve-skeleton which can be filled automatically. Since the tetrahedrization of the points on the boundary describe only the inside of the object, the algorithm can search for loose ends of the curve-skeleton and connect these if they are close to each other. In addition, it can be verified that the connection stays within the object. To test this, those tetrahedra which are close to the line connecting the two candidates and potentially filling a gap are identified. Then, the algorithm computes how much of the line is covered by those tetrahedral; i.e., the fraction of the line contained within the tetrahedra. If all those fractions add up to 1, then the line is completely within the object and it is a valid connection. Otherwise, the connection is rejected since it would introduce an incorrect connection of two independent vessels.

ACKNOWLEDGMENTS

We thank Garo Harmandayan and Brad Manubay for their technical expertise and the Wright State University and the Ohio Board of Regents for their support. This research was supported by the National Institute of Health-National Heart, Lung, and Blood Institute Grant 2 R01 HL055554-11.

REFERENCES

[1] Ahuja, N., and J. Chuang. Shape representation using a generalized potential field model. *IEEE Trans. Pattern Anal. Mach. Intell.* 19(2):169–176, 1997.

[2] Amenta, N., S. Choi, and R. Kolluri. The power crust. In: Proceedings of the 6th ACM Symposium on Solid Modeling, 2001, pp. 249–260.

[3] Aylward, S. R., and E. Bullit. Initialization, noise, singularities, and scale in height ridge traversal for tubular object centerline extraction. *IEEE Trans. Med. Imaging* 21(2):61–75, 2002.

[4] Bertrand, G., and Z. Aktouf. A three-dimensional thinning algorithm using subfields. *Vision Geom. III* 2356:113–124, 1994.

[5] Bitter, I., A. E. Kaufman, and M. Sato. Penalized-distance volumetric skeleton algorithm. *IEEE Trans. Vis. Comput. Graph.* 7(3):195–206, 2001.

[6] Bouix, S., and K. Siddiqi. Divergence-based medial surfaces. *ECCV* 1842:603–618, 2000.

[7] Brunner, D., and G. Brunnett. Mesh segmentation using the object skeleton graph. In: Proceedings of the IASTED International Conference on Computer Graphics and Imaging, 2004, pp. 48–55.

[8] Den Buijs, J. O., Z. Bajzer, and E. L. Ritman. Branching morphology of the rat hepatic portal vein tree: a micro-CT study. *Ann. Biomed. Eng.* 34(9):1420–1428, 2006.

[9] Bullitt, E., S. Aylward, K. Smith, S. Mukherji, M. Jiroutek, and K. Muller. Symbolic description of intracerebral vessels segmented from magnetic resonance angiograms and evaluation by comparison with X-ray angiograms. *Med. Image Anal.* 5(2):157–169, 2001.

[10] Canny, J. F. A computational approach to edge detection. *IEEE Trans. Pattern Anal. Mach. Intell.* PAMI-8(6):679–698, 1986.

[11] Chaturvedi, A., and Z. Lee. Three-dimensional segmentation and skeletonization to build an airway tree data structure for small animals. *Phys. Med. Biol.* 50(7):1405–1419, 2005.

[12] Cornea, N. D., D. Silver, and P. Min. Curve-skeleton applications. In: Proceedings of IEEE Visualization, 2005, pp. 95–102.

[13] Cornea, N. D., D. Silver, X. Yuan, and R. Balasubramanian. Computing hierarchical curve-skeletons of 3D objects. *Vis. Comput.* 21(11):945–955, 2005.

[14] Dey, T. K., and S. Goswami. Tight cocone: a water-tight surface reconstructor. Proc. 8th ACM Sympos. Solid Modeling Applications, 127–134. *J. Comput. Inform. Sci. Eng.* 30:302–307, 2003.

[15] Gao, L., D. G. Heath, and E. K. Fishman. Abdominal image segmentation using three-dimensional deformable models. *Invest. Radiol.* 33(6):348–355, 1998.

[16] Gill, J. D., H. M. Ladak, D. A. Steinman, and A. Fenster. Accuracy and variability assessment of a semiautomatic technique for segmentation of the carotid arteries from three-dimensional ultrasound images. *Med. Phys.* 27(6): 1333–1342, 2000.

[17] Golland, P., Eric W., Grimson W. E. L. Fixed topology skeletons. In: Proceedings of IEEE Conference on CVPR, 2000, pp. 10–17.

[18] Gong, W., and G. Bertrand. A simple parallel 3D thinning algorithm. In: IEEE Proceedings of 10th International Conference on Pattern Recognition, vol. 1, 1990, pp. 188–190.

[19] He, T., L. Hong, D. Chen, and Z. Liang. Reliable path for virtual endoscopy: ensuring complete examination of human organs. *IEEE Trans. Vis. Comput. Graph.* 7(4):333–342, 2001.

[20] Hirsch, M. W., and S. Smale. Differential Equations, Dynamical Systems and Linear Algebra. Academic Press, 1974.

[21] Jain, R., R. Kasturi, and B. G. Schunck. Machine Vision. New York: McGraw-Hill, Inc, 1995.

[22] Kaimovitz, B., Y. Lanir, and G. S. Kassab. Large-scale 3-D geometric reconstruction of the porcine coronary arterial vasculature based on detailed anatomical data. *Ann. Biomed. Eng.* 33(11):1517–1535, 2005.

[23] Kanitsar, A., D. Fleischmann, R. Wegenkittl, P. Felkel, and E. Gröller. *CPR*. Curved planar reformation. In: Proceedings of IEEE Visualization, 2002, pp. 37–44.

[24] Lee, T., R. L. Kashyap, and C. N. Chu. Building skeleton models via 3-D medial surface/axis thinning algorithms. *CVGIP: Graph. Models Image Process.* 56(6):462–478, 1994.

[25] Lobregt, S., P. W. Verbeek, and F. C. A. Groen. Three-dimensional skeletonization: principle and algorithm. *IEEE Trans. Pattern Anal. Mach. Intell.* 2(1):75–77, 1980.

[26] Lohou, C., and G. Bertrand. A 3D 12-subiteration thinning algorithm based on P-simple points. *Discrete Appl. Math.* 139:171–195, 2004.

[27] Luboz, V., X. Wu, K. Krissian, C. F. Westin, R. Kikinis, S. Cotin, and S. Dawson. A segmentation and reconstruction technique for 3D vascular structures. In: MICCAI 2005, Lecture Notes in Computer Science, vol. 3749, 2005, pp. 43–50.

[28] Malandain, G., and S. Fernández-Vidal. Euclidean skeletons. *Image Vis. Comput.* 16:317–327, 1998.

[29] Martinez-Perez, M. E., A. D. Hughes, A. V. Stanton, S. A. Thom, N. Chapman, A. A. Bharath, and K. H. Parker. Retinal vascular tree morphology: a semi-automatic quantification. *IEEE Trans. Biomed. Eng.* 49(8):912–917, 2002.

[30] Masutani, Y., H. MacMahon, and K. Doi. Automated segmentation and visualization of the pulmonary vascular tree in spiral CT angiography: an anatomy-oriented approach based on three-dimensional image analysis. *J. Comput. Assist. Tomogr.* 25(4):587–597, 2001.

[31] Nordsletten, D. A., S. Blackett, M. D. Bentley, E. L. Ritman, and N. P. Smith. Structural morphology of renal vasculature. *Am. J. Physiol. Heart Circ. Physiol.* 291(1):H296–309, 2006.

[32] Palágyi, K., and A. Kuba. Directional 3D thinning using 8 subiterations. In: Proceedings of Discrete Geometry for Computer Imagery. Lecture Notes in Computer Science, vol. 1568, 1999, pp. 325–336.

[33] Palágyi, K., and A. Kuba. A parallel 3D 12-subiteration thinning algorithm. *Graph. Models Image Process.* 61(4):199–221, 1999.

[34] Passat, N., C. Ronse, J. Baruthio, J. P. Armspach, and C. Maillot. Magnetic resonance angiography: from anatomical knowledge modeling to vessel segmentation. *Med. Image Anal.* 10(2):259–274, 2006.

[35] Passat, N., C. Ronse, J. Baruthio, J. P. Armspach, C. Maillot, and C. Jahn. Region-growing segmentation of brain vessels: an atlas-based automatic approach. *J. Magn. Reson. Imaging* 21(6):715–725, 2005.

[36] Perchet, D., C. I. Fetita, and F. Preteux. Advanced navigation tools for virtual bronchoscopy. In: Proceedings of the SPIE Conference on Image Processing: Algorithms and Systems III, vol. 5298, 2004, pp. 147–158.

[37] Saha, P. K., B. B. Chaudhuri, and D. Dutta Majumder. A new shape preserving parallel thinning algorithm for 3d digital images. *Pattern Recognit.* 30(12):1939–1955, 1997.

[38] Sauret, V., K. A. Goatman, J. S. Fleming, and A. G. Bailey. Semi-automated tabulation of the 3D topology and morphology of branching networks using CT: application to the airway tree. *Phys. Med. Biol.* 44(7):1625–1638, 1999.

[39]Schirmacher, H., M. Zöckler, D. Stalling, and H. Hege. Boundary surface shrinking – a continuous approach to 3D center line extraction. In: Proceedings of the of IMDSP, 1998, pp. 25–28.

[40]Schmitt, S., J. F. Evers, C. Duch, M. Scholz, and K. Obermayer. New methods for the computer-assisted 3-D reconstruction of neurons from confocal image stacks. *NeuroImage* 23:1283–1298, 2004.

[41]Sethian, J. A. Fast marching methods. *SIAM Rev*. 41(2):199–235, 1999.

[42]Si, H. TetGen. A quality tetrahedral mesh generator and three-dimensional delaunay triangulator. WIAS Technical Report No. 9, 2004.

[43]Spaan, J. A., R. ter Wee, J. W. van Teeffelen, G. Streekstra, M. Siebes, C. Kolyva, H. Vink, D. S. Fokkema, and E. VanBavel. Visualization of intramural coronary vasculature by an imaging cryomicrotome suggests compartmentalization of myocardial perfusion areas. *Med. Biol. Eng. Comput*. 43(4):431–435, 2005.

[44]Stefancik, R. M., and M. Sonka. Highly automated segmentation of arterial and venous trees from three-dimensional magnetic resonance angiography (MRA). *Int. J. Cardiovasc. Imaging* 17(1):37–47, 2001.

[45]Sundar, H., D. Silver, N. Gagvani, and S. Dickinson. Skeleton based shape matching and retrieval. In: Proceedings of Shape Modeling International, 2003, pp. 130–139.

[46]Telea, A., and A. Vilanova. A robust level-set algorithm for centerline extraction. In: Eurographics/IEEE Symposium on Data Visualization, 2003, pp. 185–194.

[47]Tsao, Y. F., and K. S. Fu. A parallel thinning algorithm for 3D pictures. *Comput. Vis. Graph. Image Process*. 17:315–331, 1981.

[48]Ukil, S., and J. M. Reinhardt. Smoothing lung segmentation surfaces in three-dimensional X-ray CT images using anatomic guidance. *Acad. Radiol*. 12(12):1502–1511, 2005.

[49]Wade, L., and R. E. Parent. Automated generation of control skeletons for use in animation. *Vis. Comput*. 18(2):97–110, 2002.

[50]Wan, M., F. Dachille, and A. Kaufman. Distance-field based skeletons for virtual navigation. In: Proceedings of IEEE Visualization, 2001, pp. 239–245.

[51]Wan, S. Y., A. P. Kiraly, E. L. Ritman, and W. E. Higgins. Extraction of the hepatic vasculature in rats using 3-D micro-CT images. *IEEE Trans. Med. Imaging* 19(9):964–971, 2000.

[52]Wan, S. Y., E. L. Ritman, and W. E. Higgins. Multi-generational analysis and visualization of the vascular tree in 3D micro-CT images. *Comput. Biol. Med*. 32(2):55–71, 2002.

[53]Wischgoll, T. Closed streamlines in flow visualization. Ph.D. Thesis, Universität Kaiserslautern, Germany, 2002.

[54]Zhang, L., B. E. Chapman, D. L. Parker, J. A. Roberts, J. Guo, P. Vemuri, S. M. Moon, and F. Noo. Automatic detection of three-dimensional vascular tree centerlines and bifurcations in high-resolution magnetic resonance angiography. *Invest. Radiol*. 40(10):661–671, 2005.

[55]Zhou, Y., A. Kaufman, and A. W. Toga. Three-dimensional skeleton and centerline generation based on an approximate minimum distance field. *Vis. Comput*. 14:303–314, 1998.

[56]Zhou, Y., and A. W. Toga. Efficient skeletonization of volumetric objects. *IEEE Trans. Vis. Comput. Graph*. 5(3):196–209, 1999.